Journal of
Materials Chemistry A

Materials for energy and sustainability

Accepted Manuscript

This article can be cited before page numbers have been issued, to do this please use: M. Santaya, C. Jiménez, H. E. Troiani, E. A. Carbonio, M. D. Arce, L. M. Toscani, R. Garcia-Diez, R. G. Wilks, A. Knop-Gericke, M. Bär and L. V. Mogni, *J. Mater. Chem. A*, 2022, DOI: 10.1039/D2TA02959F.

ROYAL SOCIETY OF CHEMISTRY

rsc.li/materials-a

View Article Online
DOI: 10.1039/D2TA02959F

View Article Online
DOI: 10.1039/D2TA02959F

ARTICLE

Tracking the Nanoparticle Exsolution/Reoxidation processes of Ni-doped $SrTi_{0.3}Fe_{0.7}O_{3-\delta}$ electrodes for Intermediate Temperature Symmetric Solid Oxide Fuel Cells

Received 00th January 20xx,
Accepted 00th January 20xx

DOI: 10.1039/x0xx00000x

Mariano Santaya,*[a] Catalina Elena Jiménez,**[b] Horacio Esteban Troiani,[a,c,d] Emilia Andrea Carbonio,[b,e] Mauricio Damián Arce,[a,b] Lucia Maria Toscani,[a,f] Raul Garcia-Diez,[b] Regan George Wilks,[b] Axel Knop-Gericke,[e,g] Marcus Bär,[b,h,i] and Liliana Verónica Mogni [a,d]

The development of redox stable oxide perovskite – based electrodes for cost-effective symmetric solid oxide fuel cells (SOFCs) that can work at intermediate temperatures and compete with state-of-the-art cathodes and anodes is becoming a concrete possibility. The Ni-doped STF perovskite $Sr_{0.93}Ti_{0.3}Fe_{0.63}Ni_{0.07}O_{3-\delta}$ meets such requirements by exsolving catalytically active Ni-Fe nanoparticles in reducing atmospheres that boost anode performance. This work aims at clarifying whether exsolution is a reversible process, which could extend the lifetime of SOFCs. Element-specific synchrotron – based near-ambient pressure X-ray photoelectron and absorption spectroscopies are key to understand the exsolution/reoxidation processes of the Ni-Fe nanoparticles during redox cycling the atmosphere. This study reveals that Ni exsolves easily, dragging along the more stable Fe to form nanoalloyed Ni-Fe even under mild reducing conditions. A significant Sr-surface segregation indicates that the initial Sr-deficiency cannot fully compensate for the B-site cation depletion during exsolution. Switching to oxidizing atmosphere results in a reoxidation-induced reconstruction of the electrode, in which a Fe- and Sr-rich oxide layer forms on the surface, leaving the Ni segregated from the perovskite. This reoxidized electrode shows a significantly improved cathode response in comparison to the pristine perovskite, indicating changes in the mechanisms that activate the oxygen reduction reaction.

1. Introduction

Solid Oxide Fuel Cells (SOFCs) are a key energy conversion technology for transitioning to a sustainable energy system and a hydrogen economy.[1,2] Their potential to combine with renewable systems to mitigate intermittency issues and their highly efficient energy conversion rates[3,4] make this technology unique. A SOFC device converts the chemical energy contained in a fuel such as H_2 or lower hydrocarbons into electricity, while co-generating high-quality heat.[5] SOFC devices present several advantages from different standpoints: they can reduce greenhouse gas emissions per generated kWh, their power output can be tuned depending on the desired application, and under reverse operation conditions they are able to produce fuels by electrolysis (i.e., when employed as electrolyzers).[6] Despite the advantages, widespread use is encumbered by the high operation and maintenance costs linked to the high operation temperatures (800 – 1000 °C) and the aggressive reducing/oxidizing atmosphere conditions that promote degradation mechanisms. The scientific community is continually studying strategies to cope with these problems. Some of these strategies consist of reducing the operation temperature to the so-called Intermediate Temperature region between 500 – 700 °C (IT-SOFC) in order to mitigate degradation phenomena,[7] or designing smart materials[8] that take advantage of the changes induced under operating conditions in either a Symmetric design, using the same material as cathode and anode and switching the atmosphere (S-SOFC) or Reversible operation, switching between fuel cell and electrolyzer operation (R-SOFC).

Perovskite-type oxides (ABO_3) are ideal for exploring these different strategies given that their composition can be widely tuned to gain electrocatalytic functionalities.[9,10] Mixed ionic

[a] Departamento Caracterización de Materiales, INN-CNEA-CONICET, Av. Bustillo 9500, Bariloche, Rio Negro, 8400, Argentina.
[b] Helmholtz-Zentrum Berlin für Materialien und Energie GmbH, Albert-Einstein-Str.15, 12489, Berlin, Germany
[c] Universidad Nacional de Río Negro, Río Negro, Argentina
[d] Instituto Balseiro, Universidad Nacional de Cuyo, R8402AGP San Carlos de Bariloche, Argentina
[e] Fritz-Haber Institute, Dept. of Inorganic Chemistry, Faradayweg 4, 14195 Berlin, Germany
[f] Instituto de Tecnologías Emergentes y Ciencias Aplicadas (ITECA), UNSAM-CONICET, Escuela de Ciencia y Tecnología, Laboratorio de Cristalografía Aplicada, Av. 25 de Mayo 1169, 1650 San Martín, Provincia De Buenos Aires, Argentina
[g] MPI for Chemical Energy Conversion, Stiftstrasse 34 – 36, 45470 Mülheim an der Ruhr, Germany
[h] Friedrich Alexander Universität Erlangen-Nürnberg, Egerlandstr. 3, 91058 Erlangen, Germany
[i] Helmholtz Institute Erlangen-Nürnberg for Renewable Energy (HI ERN), Albert-Einstein.Str. 15, 12489 Berlin, Germany
* Corresponding author1: marianosantaya@gmail.com
** Corresponding author2: catalina.jimenez@helmholtz-berlin.de
Electronic Supplementary Information (ESI) available: [details of any supplementary information available should be included here]. See DOI: 10.1039/x0xx00000x

electronic conducting (MIEC) perovskites have been widely studied as IT-SOFC cathodes[11] and perovskites that are stable under reducing conditions has also been proposed[12] as replacements for the traditional Ni-YSZ composite anode materials to improve redox stability and mitigate coking when using C-containing fuels, although their electrocatalytic efficiency is still lower than that of Ni-composite anodes. Surface functionalization of MIEC perovskites can help to improve electrode performance, e.g., by forming nanoparticles on their surface through B-site differential diffusion under reducing environmental conditions – the so-called exsolution process. These exsolved nanoparticles can enhance the electrocatalytic activity of the anode for fuel dissociation,[13–15] improve C-tolerance[16] and reduce particle coarsening, because the nanoparticles are anchored to the perovskite surface and grain boundaries.[17,18] It is a complex task to fully understand the exsolution process, since it depends on several factors: A-site deficiency,[19–21] transition metal B-site doping degree,[22] original material microstructure (grain size and defect structure),[23] and external exsolution conditions such as temperature,[24,25] atmosphere[26] or applied cell voltage.[27] Also, whether or not exsolution is reversible when switching to oxidizing atmosphere has been recently debated. Strategies for regenerating materials upon atmosphere switching are particularly interesting for S-SOFC, which requires redox stable materials with good activity for both fuel oxidation and oxygen reduction reactions.[28] In the search for materials that meet such requirements, strontium titanium ferrite ($SrTi_{0.3}Fe_{0.7}O_3$, STF) and Ni-doped STF were recently found to have outstanding performance both as anode[14,21] after exsolution and cathode after reoxidation.[29] Cells with $Sr_{0.95}Ti_{0.3}Fe_{0.63}Ni_{0.07}O_3$ anode were recently reported to achieve a 0.95 W cm^{-2} power density at 800 °C in humidified hydrogen (with LSGM electrolyte, LDC buffer layer and LSCF-GDC cathode)[14], and a cell with $Sr_{0.95}Ti_{0.3}Fe_{0.6}Ni_{0.1}O_3$ cathode exhibited a maximum power density of 0.74 W cm^{-2} operating at 750 °C (YSZ electrolyte and Ni-YSZ anode)[30]. These results position Ni-doped STF materials as very promising electrodes for S-SOFC.

At present, the optimized nanostructured electrode material studied in this work has the composition $Sr_{0.93}Ti_{0.3}Fe_{0.63}Ni_{0.07}O_3$ (STFN). The Sr-deficiency is meant to stabilize the perovskite structure by compensating for the necessary B-site depletion that occurs during exsolution, intending to prevent excessive Sr segregation.[21,31] However, a characterization of the surface chemistry and oxidation states of the transition metals at the solid/gas interface during operation that could provide a mechanistic description of the interplay between exsolution and surface Sr enrichment or limiting steps of the solid/gas reaction is still lacking. Moreover, it is not known whether exsolution in STFN is sufficiently reversible to enable a material regeneration by reoxidation. The heterogeneous nature of these surface phenomena requires very surface-sensitive and element-specific techniques such as synchrotron-based near-ambient pressure X-ray photoelectron and absorption spectroscopies (NAP-XPS and NAP-XAS). These techniques proved effective to in-situ study the exsolution[25,27] or degradation processes through surface Sr segregation[32,33] on other perovskite electrode materials under atmospheres and temperatures that are truly relevant for the application.

In order to gain insights into the exsolution process of STFN and its reversibility for exploring the feasibility of STFN regeneration, this work focuses on following changes in-situ as induced by changing between reducing and oxidizing atmospheres. Synchrotron-based NAP-XPS and NAP-XAS will be exploited to in-situ characterize the surface chemistry of STFN, identifying chemical species, oxidation states, and the electronic structure at the solid/gas interface. Depth-dependent NAP-XPS is additionally used to understand structure profile modifications induced by atmosphere changes and, in combination with electrochemical impedance spectroscopy (EIS), to provide a mechanistic understanding of the electrochemical solid/gas reaction on STFN electrodes. Complementary scanning and transmission electron microscopy analysis including energy dispersive X-ray spectroscopy (EDS) will provide access the microstructural evolution and local nanoparticle composition.

2. Results

2.1 Mass change during redox cycle and its effect on microstructure

Figure 1 shows thermogravimetric (TG) analysis for the STFN pellet during the redox cycle, accompanied by SEM and TEM images portraying the microstructural evolution of the electrode surface on each step of the process. The mass of the TG curve in Figure 1.a is normalized to the mass of the pristine sample in air at 700 °C defined as m_0. A first step of the reduction process occurs when the chamber is purged with Ar and (i) cations in the perovskite are partially reduced (Fe^{+4}/Fe^{+3} to Fe^{+3}/Fe^{+2}) due to a decrease in the partial pressure of oxygen (pO_2). The observed mass loss is caused by oxygen leaving the lattice as a consequence of the cation reduction. Afterwards, the atmosphere is changed to a $10\%H_2/3\%H_2O/87\%Ar$ reducing condition and reduction proceeds in two simultaneous steps: (ii) a further reduction of the perovskite redox active cation increasing the Fe^{+2} content and (iii) the complete reduction of Ni^{+2} to Ni^0 (and a portion of iron) via exsolution of metallic nanoparticles. Ad hoc TPR measurements comparing hydrogen consumption by STF and STFN vs. temperature indicate a three-step reduction profile for STFN in which Ni lowers the temperatures for the reduction steps of iron species with respect to STF (Figure S1, SI). The presence of exsolved nanoparticles (~10 nm) of a Ni-Fe alloy (with $\sim Ni_{0.7}Fe_{0.3}$ composition according to TEM-EDS and $\sim Ni_{0.6}Fe_{0.4}$ composition according to the XRD lattice parameter in Figure S2, SI) decorating the surface is confirmed in the reduced STFN (Figure 1.c), in contrast to the clean (i.e., nanoparticle-free) surface of the pristine STFN (Figure 1.b). Exsolution is seen to occur at relatively low temperatures for this sample investigated at 700 °C, compared to many previous works where reduction is reported to require more aggressive conditions,[14,19,34] i.e., higher temperature, higher partial

View Article Online
DOI: 10.1039/D2TA02595E

pressure of hydrogen (pH_2), and/or longer reduction times. Regions highlighted with squares in the SEM images in Figure 1.c and Figure 1.d indicate that a few small Ni particles, not incorporated to the perovskite during the synthesis, are also reduced in this condition (as confirmed by SEM-EDS in Figure S3, SI). After reducing the sample for 4 h (time = 7.5 h) the chamber is again purged with Ar. Then the sample is reoxidized in air, and within 9 minutes of reoxidation the sample mass rebounds to a mass fraction of m/m0 = 0.998 (see Figure 1.a), i.e., very close to the initial mass. It becomes obvious that reoxidation is a faster process than reduction, but during reoxidation the sample does not fully recover the mass of the pristine condition, even after 24 h. The micrographs given in Figure 1.d show that after 1 h reoxidation the sample surface is still very different from that of the pristine STFN. Oxide nanoparticles of size ~20 nm can be found, their composition being mainly NiO with very low Fe content as obtained from the TEM-EDS analysis, which is compatible to the crystalline structure of NiO. These reoxidized $(Ni,Fe)O_x$ nanoparticles are more sparsely distributed than the metallic nanoparticles in the reduced sample. Also, prominent "ledges" can be seen all over the sample surface contrasting with the soft surface observed in pristine STFN. After 24 h of reoxidation, no nanoparticles are found, although the surface "ledges" remain.

2.2 Electrochemical characterization of STFN as electrode for S-SOFC

Figure 2 and 3 summarize the electrochemical responses of STFN as cathode and anode, respectively, as evaluated by EIS

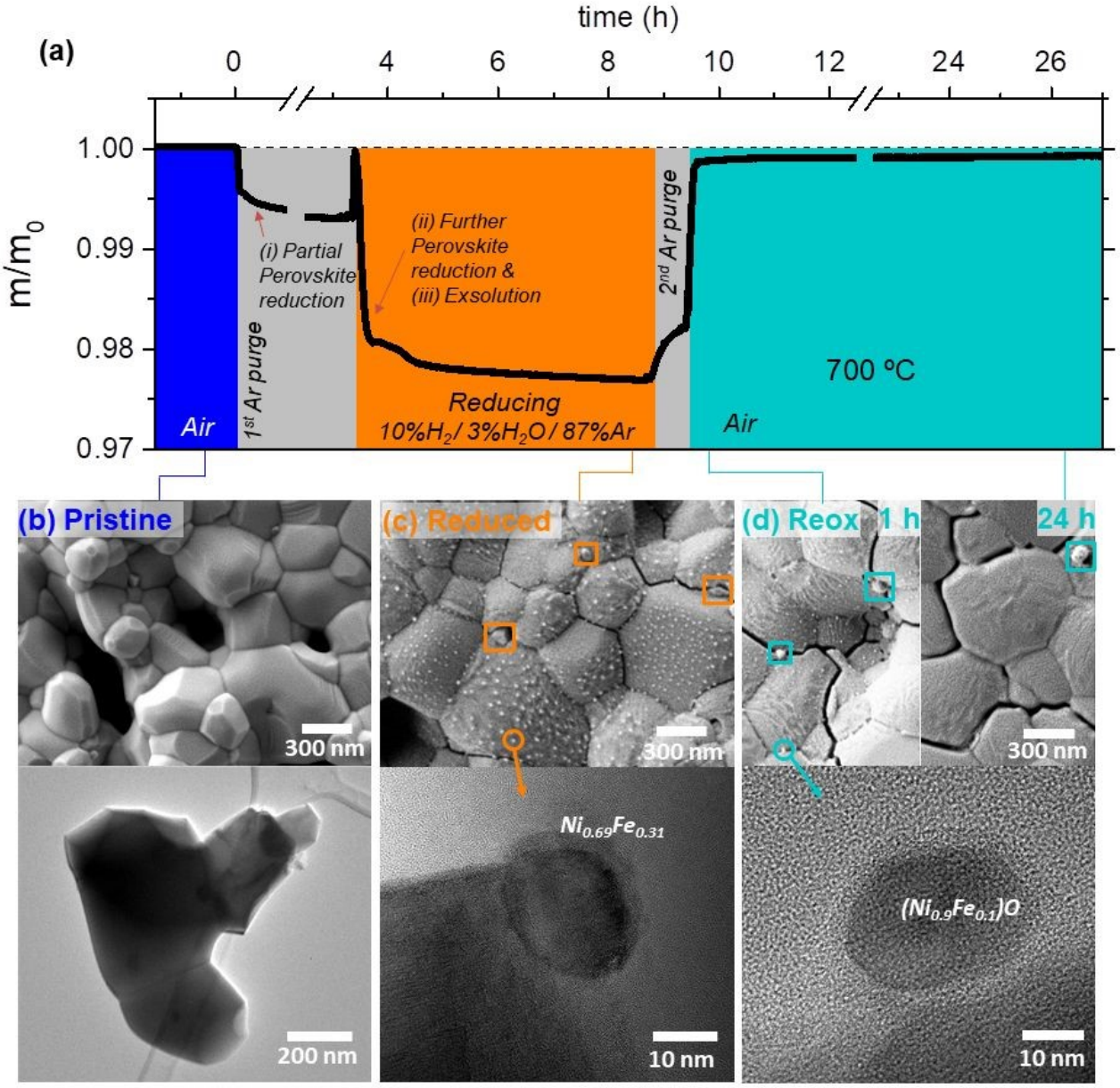

Figure 1. (a) Thermo-gravimetric study of a reduction/oxidation cycle normalized to the original mass in air at 700 °C. Reduction was carried out at 700 °C in a 50% H2 humidified atmosphere and reoxidation was performed in air. The panels below show SEM (top) and TEM (bottom) images of the STFN (b) pristine, (c) after 4 h reduction and (d) after 1 h and 24 h reoxidation. Ni and Fe atomic proportions on metallic NPs were determined by TEM-EDS analysis.

View Article Online
DOI: 10.1039/D2TA02595E

in relation to the reversibility of the exsolution process during a redox cycle towards its possible use as S-SOFC electrode. Both Figure 2 and 3 include the adopted electrical equivalent circuits (EEC) used to fit the EIS spectra. Each circuit element represents a process taking place during the fuel oxidation in the anode and the oxygen reduction in the cathode, namely surface adsorption and molecule dissociation of the reacting species, ionic or gas diffusion, etc. These distinctive processes are usually separated according to their characteristic frequency or relaxation times, their temperature and pO_2/pH_2 dependence.

Figure 2 shows the Nyquist and Bode plots corresponding to the STFN cathode supporting the oxygen reduction reaction (ORR) in air at 700 ºC. Figure 2.a corresponds to the STFN pristine and Figure 2.b corresponds to the same reoxidized electrode with its response plotted at different reoxidation times. All measurements were fitted with the same EEC as shown in the inset of Figure 2.a, which includes a low-frequency arc assigned to a resistance in parallel with a pseudocapacitance (RCP) and a high-frequency arc fitted with a Gerischer-type element (G). The need for a diffusive Gerischer-type element in the HF arc becomes clearer in the lower temperature spectra, in which the 45° slope at high frequencies is more evident (see Figure S4 of SI). It can be seen that while the RCP arc remains practically unchanged from pristine to reoxidized conditions, G decreases and shifts towards higher frequencies (indicating faster reaction times). The low-frequency arc is not only unaltered after reduction but shows almost no temperature dependence (Figure 2.c and 2.d), which is the typical behavior of O_2 diffusion in the gas phase. Also, this contribution in the EIS spectrum becomes negligible at 700°C in pure O_2, verifying this hypothesis (Figure S5, SI). The high-frequency (>100 Hz) Gerischer-type impedance is typical of diffusion processes of O-species either on the surface or in the bulk of the electrode.[35] In this case, the G pseudocapacitance presents values ranging from 10^{-1}-10^{-2} F.cm^{-2}, which are in between the values for a bulk and a

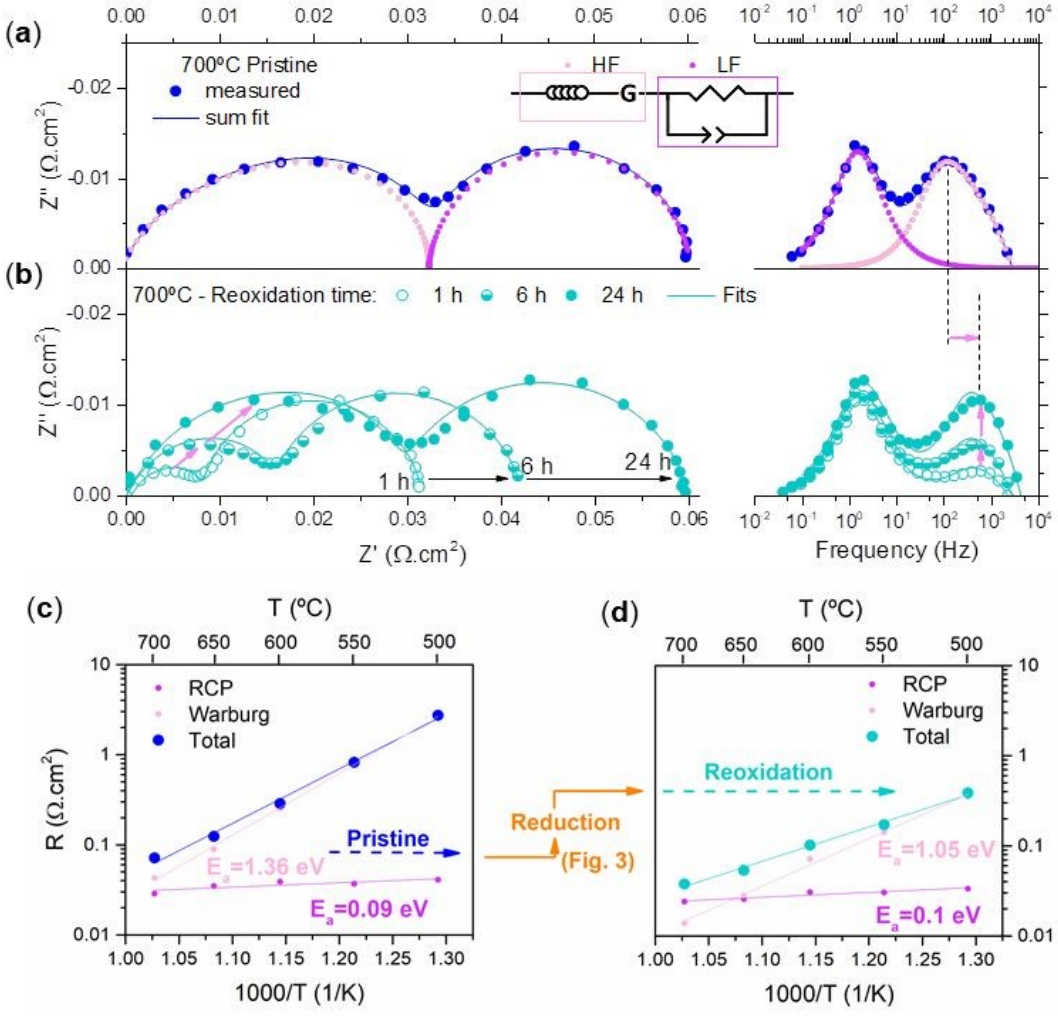

Figure 2 Nyquist and Bode plots of the normalized EIS data for the symmetrical cell working as cathode with (a) STFN pristine electrode prior to reduction, and (b) STFN reoxidized in air at 700 ºC for different reoxidation times. The equivalent circuit model is also shown in (a) and the contribution of each circuit element is plotted along with the sum fit. Arrhenius plots are shown in panels (c) and (d) for the STFN pristine and reoxidized (after reduction) respectively, to show the temperature dependencies of each arc and the total contributions.

surface process [36] (the expressions used for the RCP and G elements, and the estimates of capacitance values, are described in section S3 of SI). In Figure 2.b it can be seen that after only ~1 h reoxidation, the G arc presents very small resistance and the O_2 gaseous diffusion process is the main limiting step. However, the high-zfrequency response continues to increase with reoxidation time, until after 24 h the total resistance is again similar to that of the pristine STFN sample. This is consistent with the fact that the surface of the STFN changes with reoxidation time, as can be observed in the SEM images of Fig. 1. The frequency shift to higher frequencies (~500 Hz) remains constant regardless of the reoxidation time and does not tend to recover its original pre-exsolution values (~100 Hz). This indicates that the reoxidation process is not completely reversible, in agreement with microstructural changes observed in Figure 1. Further discussion on the mechanisms of the ORR is given in section (3.3).

Figure 3.a shows Nyquist and Bode plots of the EIS response towards the Hydrogen Oxidation Reaction (HOR) of the symmetrical cell working as anode at 700 ºC in a wet 10% H_2 atmosphere (reduced). In contrast to the cathodic processes, the anodic response seems to be more complex (compare Figures 2 and 3). In fact, the Distribution of Relaxation Times (DRT) calculation shown in panel (c) reveals the presence of four main processes for the spectra measured at 700 °C, ranging from low frequencies (LF~1-0.1 Hz) to ultra-high frequencies (UHF~10^3-10^4 Hz). Based on this, the EEC model proposed in panel (a) is composed of a high frequency inductance and three RCP elements connected in series with a Gerischer circuit element, where the latter accounts for the broad peak in the high frequency (HF) arc. Figure 3.b shows the Arrhenius type dependencies of these different contributions between 550 and 700 ºC. Figure 3.c also shows DRT calculations for EIS spectra measured at the indicated temperatures, all measured in wet 10% H_2 atmosphere. The MF response shifts to lower frequencies as temperature decreases, and eventually merges with the LF response, making it difficult to deconvolute these two contributions below 600 °C. For this reason, the sum of the MF and LF arcs together is used in the Arrhenius plot in panel (b). The HF region, represented in grey in panel (c), was fitted with a unique Gerischer element up to 600 ºC and an extra RCP_{HF} was added at 550 ºC to account for the HF region broadening at low temperatures. Since at 550 ºC only one RCP was used for the MF+LF region, the ECC still consisted of three RCP in series plus a Gerischer element.

The UHF and HF responses range between 10^5 to 10^2 Hz and are typically associated with charge transfer processes such as ion transfer between electrode/electrolyte interface[37], O^{2-} ion bulk diffusion processes [38] and electron transfer in the hydrogen oxidation reaction [37]. The characteristic frequency and resistance of the UHF process drops as temperature decreases, in a similar fashion compared to reports of other similar perovskites.[38,39] Note also that the UHF+HF contributions are more resistive in the fuel electrode compared to the air electrode. This is probably related with the electrical conductivity, which for STF [40–42] and other similar perovskites [15,39,43] is lower in reducing atmospheres.

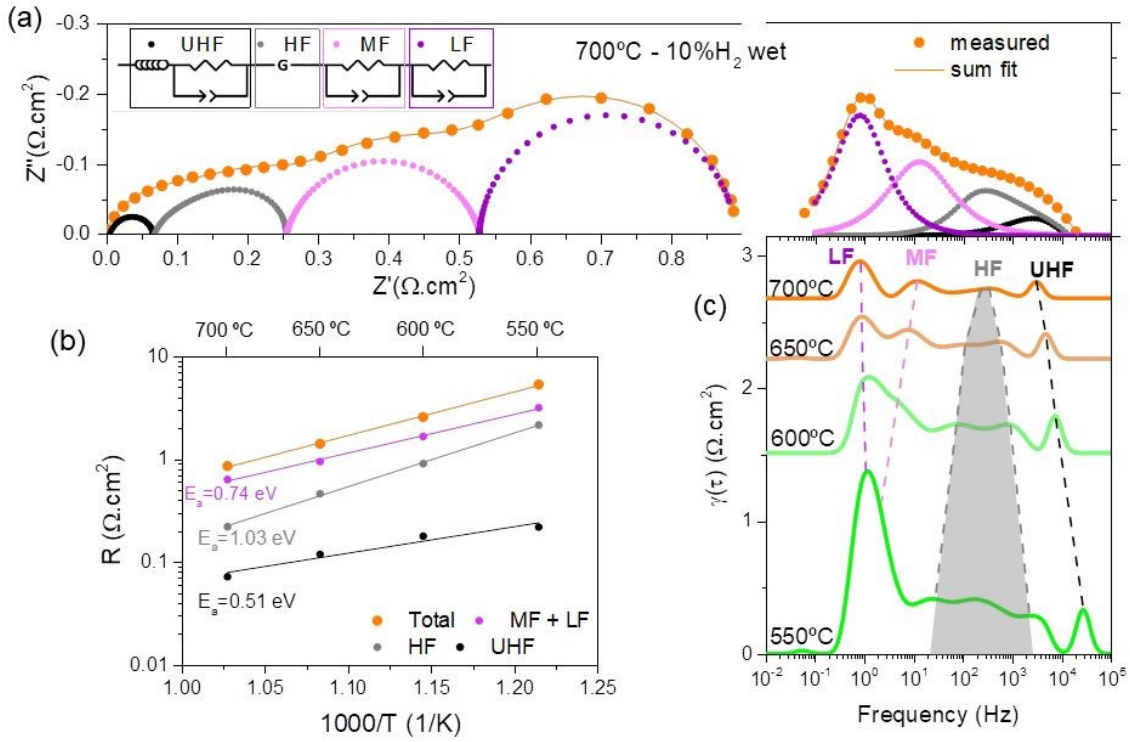

Figure 3(a) Nyquist and Bode plots of the normalized EIS response of the STFN symmetrical cell at 700 ºC in a wet 10% H_2 atmosphere. The EEC model used for fitting is also shown in the inset and the contribution of each circuit element is plotted along with the sum fit. (b) Arrhenius plot of the different contributions separated from low frequencies (LF) to ultra-high frequencies (UHF). (c) Distribution of Relaxation Times (DRT) calculated from spectra measured at different temperatures.

The MF arc has frequency values of ~10^1 Hz at 700°C, and capacitance values of ~5.10^{-2} F.cm^{-2}, and the LF is centered in ~0.8 Hz in frequency, with capacitances of ~6.10^{-1} F.cm^{-2}. Such low frequencies and high capacitance values have previously been observed on similar STF[44] and STFN[14] perovskite anodes, as well as in chromite[45,46] and ferrite anodes [37,47], and have been associated with (i) H_2 diffusion in the gas phase[43,48] or (ii) H_2 adsorption/dissociation,[38,39,45] as well as a combination of all these processes.[37,47] In our case, given that the same electrode was tested as cathode and anode and that the LF cathode contribution was identified to be due to O_2 gaseous diffusion, we should expect a resistance value for H_2 gas diffusion in the anodic condition at least ~4 times lower than in the cathodic one, due to the higher H_2 diffusion coefficient. Therefore, the higher LF impedance suggests that another process is also contributing to this LF arc. In conclusion, the MF+LF arcs in Figure 3.a can be ascribed to H_2-dissociative adsorption processes. The separation of the LF region into two LF+MF arcs, in connection with the mechanisms of the HOR is further discussed in section (3.3).

2.3 Surface chemistry evolution followed in-situ by NAP-XPS and NAP-XAS – NP exsolution, Sr segregation and reoxidation

2.3.1 Surface chemical states and valence band changes induced by redox cycling the atmosphere. Figure 4 presents the changes in the most relevant core level NAP-XPS spectra of STFN: Ni 2p + Fe 2s, Fe 2p, O 1s, Ti 2p, Sr 3d, and valence band region in the pristine, reduced and reoxidized conditions that are induced by redox cycling the 0.5 mbar atmosphere at 700 °C. Considering that all the NAP-XPS spectra in Figure 4.a. – .e were acquired with photoelectrons of ~150 eV kinetic energy, corresponding to an inelastic mean free path (IMFP) of ~0.58 nm, [49] and that the lattice parameter of the pristine perovskite is 0.38 nm [50], one can say that these NAP-XPS spectra describe the surface chemical states on a region that hereafter is referred to as the *termination layer*. The core levels of the non-redox active elements Sr 3d, Ti 2p and O 1s undergo reversible shifts in binding energy ΔE_b of 0.8 – 1.0 eV when the atmosphere is redox cycled (Figure 4.c – .e). These ΔE_b relate to a shift of the perovskite's Fermi level induced by the Δp

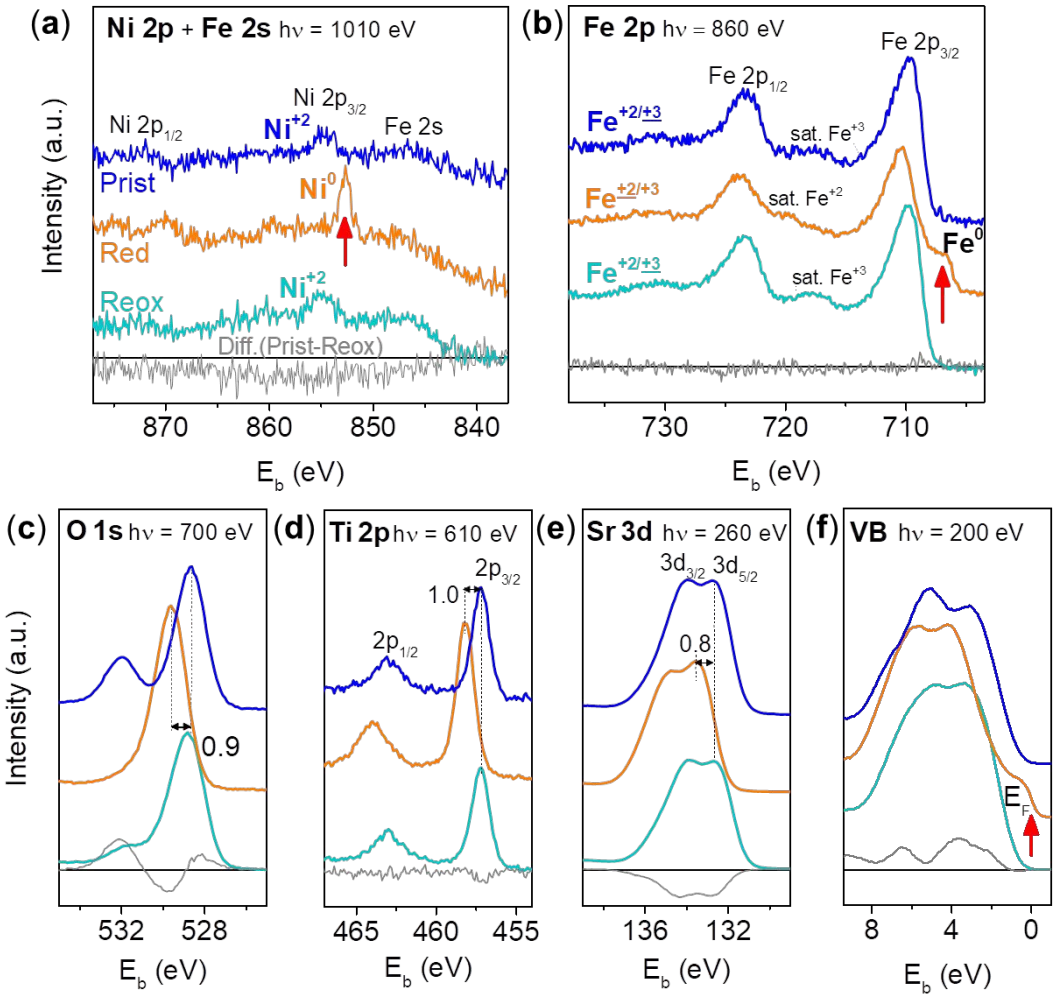

Figure 4 a – .f. NAP-XPS spectra of Ni 2p + Fe 2s, Fe 2p, O 1s, Ti 2p, Sr 3d core levels and the valence band of STFN pellets acquired in-situ at 700°C in 0.5 mbar of oxidizing and reducing atmospheres. Each panel compares the pristine, reduced, and reoxidized conditions. The intensity difference between pristine and reoxidized conditions indicated as Diff. (Prist.)-(Reox.), is also included. The color code applies to all regions.

View Article Online
DOI: 10.1039/D2TA00595

(O_2) between oxidizing and reducing atmospheres that also affects the chemical potential (see details in section S4.1 of SI). Similar shifts were reported for other STF perovskites in literature[27,41]. In the spectra of the redox-active species Ni 2p + Fe 2s and Fe 2p, the shift towards lower E_b when switching to reducing atmosphere is less obvious due to the concurrent appearance of metallic Fe and Ni spectral signatures associated with the exsolved Fe-Ni NPs (Figure 4.a and .b). In addition, satellite features in the Fe 2p region indicate an increased presence of Fe^{+2} in the perovskite in reducing atmosphere compared to the predominance of Fe^{+3} in oxidizing atmospheres. In the valence band the exsolution leads to the formation of a Fermi edge (E_F, Figure 4.f), corroborating the presence of metallic species. The intensity difference spectra between pristine and reoxidized conditions (Diff. (Prist-Reox) curves) suggest that the redox cycle induces some irreversible changes in the surface chemistry of STFN. Elemental depth distributions of Sr and O and oxidation states of Ni and Fe, complemented by the analysis of NAP-XAS spectra, during the atmospheric redox cycle are included in the next two sections.

2.3.2 Analysis of Sr and O profile. Figure 5.a and 5.b display exemplary NAP-XPS spectra of the Sr 3d and O 1s core levels, respectively. Again the photon energy was chosen such that the kinetic energy of the recorded photoelectrons was 150 eV, resulting in an IMPF of ~0.5 nm. The detailed fit analysis of the spectra indicates the presence of three components for both elements. The low binding energy compound is ascribed to represent the chemical environment in the "bulk", whereas the two high-binding energy components are attributed to the chemical environment at the "surface" (see also Figures S6 and S7 of the SI for information on the fitting models). Note that a broader peak shape for the fit of the surface contributions was employed assuming a larger disorder (due to differences in bond angles and bond length) at the surface. The respective 400 eV (IMFP of ~1.0) and 700 eV (IMFP of ~1.5 nm) kinetic energy Sr 3d and O 1s spectra, respectively, can be found in Figure S8 and S9 of the SI. In the spin-orbit split Sr $3d_{3/2}$ and $3d_{5/2}$ spectra in Figure 5.a the bulk doublet is ascribed to Sr in the perovskite lattice (E_b ~ 132.4 eV for the pristine STFN), whereas the two surface doublets are attributed to SrO or $Sr(OH)_2$ species, as previously reported.[27,32,33,51] Since no C species were detected at 700 °C under the applied atmospheres (see Figure S10, SI) Sr carbonate or oxalate can be neglected as possible surface species. In Figure 5.b, the O 1s bulk singlet is ascribed to oxygen in the perovskite lattice (E_b ~ 528.6 eV for the pristine STFN). Also, there are two O 1s surface singlets at ~530 eV and at ~532 eV (pristine STFN). The one at ~530 eV denoted as M-O represents oxygen from OH^- or O^{2-} bonded to a metal in the perovskite's termination layer (with M being Sr and/or one of the transition metals).[52–54] The one at ~532 eV E_b is attributed to chemisorbed oxygen (O_{ads})[52–54] that can be assigned to $\mathbf{OH^-_{ads}}$, $\mathbf{O^-_{ads}}$ or $\mathbf{O^-_{2,ads}}$ in that order with E_b being reported within 530 – 533 eV, given the fact that oxygen reduction takes place in several steps.[52–54] The binding energies suggest that on the pristine perovskite more weakly bound $\mathbf{O^-_{2,ads}}$ predominate as adsorbed surface species (E_b ~532.0 eV) whereas on the reoxidized surface dissociated $\mathbf{O^-_{ads}}$ takes over (E_b~531.5 eV).[54] These results are further discussed in section 3.3.

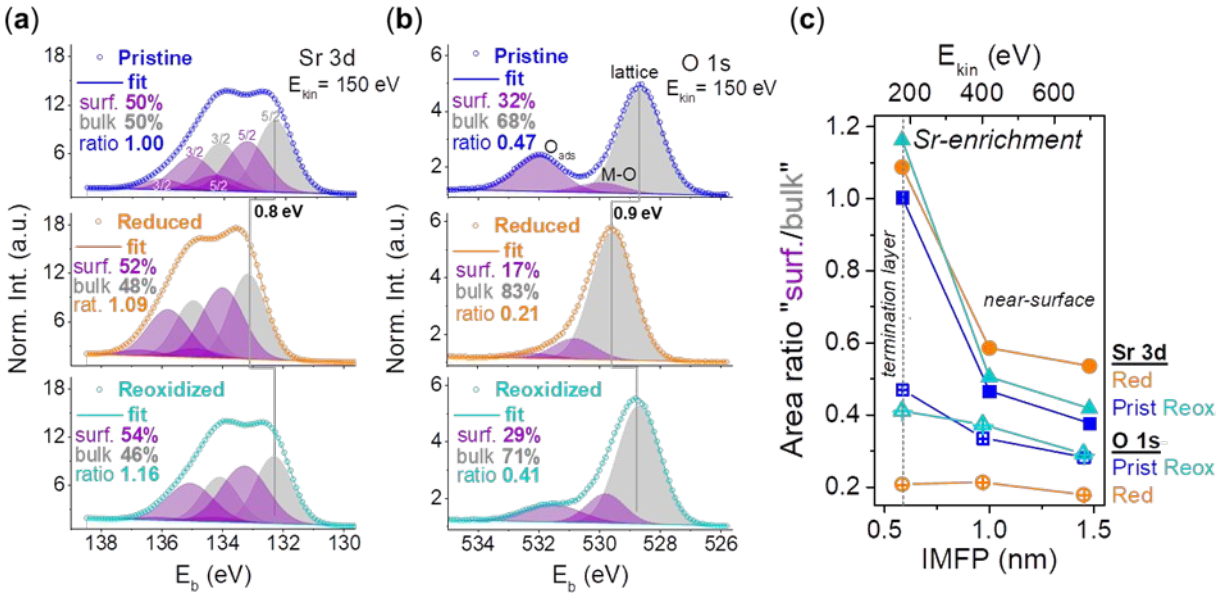

Figure 5 (a) Sr 3d and (b) O 1s NAP-XPS spectra acquired at 700 °C while following changes induced by cycling between reducing and oxidizing atmospheres. Assumed bulk and surface species in the pristine, reduced and reoxidized conditions are indicated. Both (a) and (b) show the set of fitted spectra acquired with photon energies selected such that the kinetic energy of the recorded photoelectrons results in the same value: ~150 eV (IMFP ~ 0.5 nm). Similar spectra were also acquired with photoelectrons of 400 and 700 eV kinetic energy for structure profile analysis, see Figure S8 and S9 of SI. (c) Summary of all surface/bulk area ratios of the Sr 3d and O 1s spectra as a function of photoelectron's kinetic energy (and thus IMFP).

Figure 5.c summarizes the chemical structure profile as a function of the IMFP in the pristine, reduced and reoxidized conditions. It can be observed that with an increasing IMFP, the surface species become less prominent, resulting in a lower "surface/bulk" ratio. In Figure 5.c the region beneath the termination layer is defined as the near-surface region (IMFP between 1.0 – 1.5 nm). Interestingly, when the sample is reduced, there is an overall Sr enrichment (i.e., in the termination layer as well as in the near-surface region) compared to the Sr content of the STFN pristine indicated by an increased "surface/bulk" ratio. The Sr 3d "surface/bulk" ratio in the termination layer of the reoxidized sample does not recover its original value, however, it approaches the value of the pristine STFN in the near surface region, where the redox cycle tends to be more reversible.

For the O 1s spectra, the "surface/bulk" ratio decreases in reducing atmosphere indicating the loss of O_{ads} and the formation of oxygen vacancies ($V_{\ddot{O}}$) both in the termination layer and in the near surface region, which is reasonable for the lower pO_2 being present in reducing conditions. Upon reoxidation, the oxygen surface/bulk ratio increases to that of the pristine sample in the near surface region, but does not quite reach the initial state in the termination layer (Figure 5.c). However, the O 1s contribution attributed to $O_{M\text{-}O}$ species in reoxidized conditions increases with respect to the pristine condition (Figure 5.b), which can be related to the above-discussed Sr surface enrichment present in the form of SrO in the termination layer. This is also in line with the seemingly more reversible behavior of the "surface/bulk" ratio observed in the "near surface" region" compared to that in the termination layer. Therefore, the net reduction of the "surface/bulk" ratio for O 1s in the reoxidized termination layer in comparison to the pristine condition is due to a change in the nature and concentration of the O_{ads} species.

2.3.3 Tracking oxidation states and chemical species of Fe and Ni. Figure 6.a compares Ni L-edge spectra of STFN with the ones of reference materials NiO (for Ni^{2+}) and Ni foil (for Ni^0) measured by NAP-XAS in total electron yield (TEY) detection mode during the redox atmosphere cycle. The presented data are normalized to go from 0 (pre-edge) to 1 (post-edge) using the software Athena. [55] The shapes of the Ni L-edge in the pristine and reoxidized conditions resemble the Ni^{+2} reference spectrum. Ni^{+2} has a characteristic unfolding of the main L_3 and L_2 absorption edges into *double features*, where the smaller feature appears as Ni acquires extra electrons from the O 2p states.[56] Note that the differing L_2/L_3 intensity ratio is due to the significantly increased Ni content in NiO compared to that in STFN. In reducing atmosphere, the Ni spectrum resembles that of the Ni^0 reference spectrum. Ni^0 is (i) less intense than Ni^{+2} because of a higher e^- occupancy of the 3d level, and thus a lower amount of 2p→3d transitions, and (ii) it presents a characteristic satellite feature ~ 6 eV above the main L_3 peak, also observed in references [57,58] and in our Ni^0 spectrum. The NAP-XAS in auger electron yield (AEY) detection mode spectra shown in Figure 6.b confirm that in oxidizing conditions Ni is present as Ni^{+2}, whereas in reducing atmosphere it is present as Ni^0. As the AEY spectra are more surface sensitive than the TEY [59], the comparison provides some insight in the time evolution of Ni-related chemical changes at the surface. The change from Ni^{+2} to Ni^0 when shifting from oxidizing to reducing conditions occurs right from the start, even under 10 $\%H_2$. Increasing to 50 $\%H_2$ does not change the spectrum, which suggests that Ni reduction during exsolution is fast and complete. When reoxidation starts, the oxidation state of Ni reverts to Ni^{+2}, but the intensity of the Ni L edge is considerably higher than that of the pristine perovskite, which points at a Ni migration to the surface during exsolution. After 3 h of reoxidation the intensity of the Ni L-edges again decreases (see arrow in rightmost panel Figure 6.b), suggesting

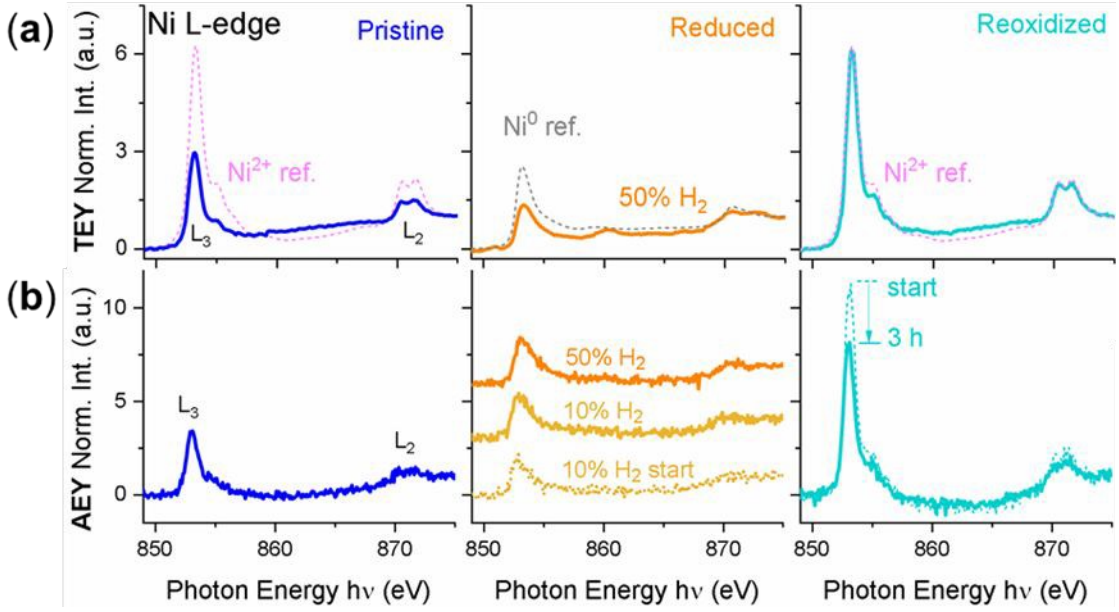

Figure 6 Ni L-edge NAP-XAS: (a) TEY signal measured for the pristine, reduced and reoxidized STFN pellet, along with that of a NiO (Ni+2) and Ni foil (Ni0) reference for comparison, and (b) AEY signal following the atmosphere/time evolution for the reduction and reoxidation processes.

that Ni^{+2} partially reincorporates in the perovskite lattice. Yet the intensity of the Ni L edge NAP-XAS spectrum after 3 h is still larger than that of the pristine perovskite, indicating a higher concentration of Ni on the final reoxidized surface.

Next, we will discuss the Fe L-edge NAP-XAS spectra of the STFN pellet at 700°C during the redox cycle to further sharpen the description of the NP exsolution and reoxidation processes. Figure 7.a and .b show selected AEY and TEY Fe L_3-edge NAP-XAS spectra together with a linear combination analysis (LCA) based on the respective spectra of reference compounds Fe foil (Fe^0), FeO (Fe^{+2}), and Fe_2O_3 (Fe^{+3}), see Figure S11, at the indicated times and atmospheres. On the surface of the electrode, Fe is present in Fe^{+2} + Fe^{+3} oxidation states as under oxidizing atmosphere and with an additional Fe^0 contribution from the exsolved metallic NP under reducing atmosphere, in agreement with the NAP-XPS spectra of the Fe 2p region in Figure 4.b. XAS is not only sensitive to the oxidation state but also to the coordination number of the probed sample:[60] here we assume that Fe is found only in octahedral sites (as is also the case for the used references). However, the presence of O vacancies on the surface may result in the formation of a surface tetrahedral coordination[61] which may affect the XAS signal. Thus the LCA-derived composition stated in Figure 7 has inherent limitations and thus is used rather to illustrate the trends during the redox cycle rather than determining absolute compositions in the following. The larger contributions of Fe^{+2} and Fe^0 to the AEY (compared to the TEY) spectra indicate that Fe is more reduced in the termination layer independent of atmosphere. Obviously, the percentage of Fe^{+3} is larger in the TEY (than the AEY) spectra as the former is less surface sensitive.

Figure 7.c condenses the LCA results of all AEY spectra by means of metallic (Fe^0) and oxidized (Fe^{+2}+Fe^{+3}) iron composition vs. time during the whole redox cycle. Fe^0 is already detected when reducing under an atmosphere containing 10% wet H_2 , but the percentage significantly increases when turning to a more reducing condition with 50% wet H_2, reaching a plateau within approximately 1h. Contrarily, as reoxidation starts Fe^0 disappears immediately (similarly to what was observed by TG analysis, Figure 1). Also, the percentages of Fe^{+2} and Fe^{+3} of the pristine and reoxidized spectra are very similar, indicating reversibility and, possibly, that Fe is more likely to be reincorporated in the perovskite than Ni after 3 h of reoxidation. This is consistent with the chemical compositions of the NP determined by TEM-EDS in which the remaining reoxidized NP appeared to be richer in Ni ($Ni_{0.9}Fe_{0.1}$) than were the freshly exsolved NP (~ $Ni_{0.7}Fe_{0.3}$), see Figure 1.

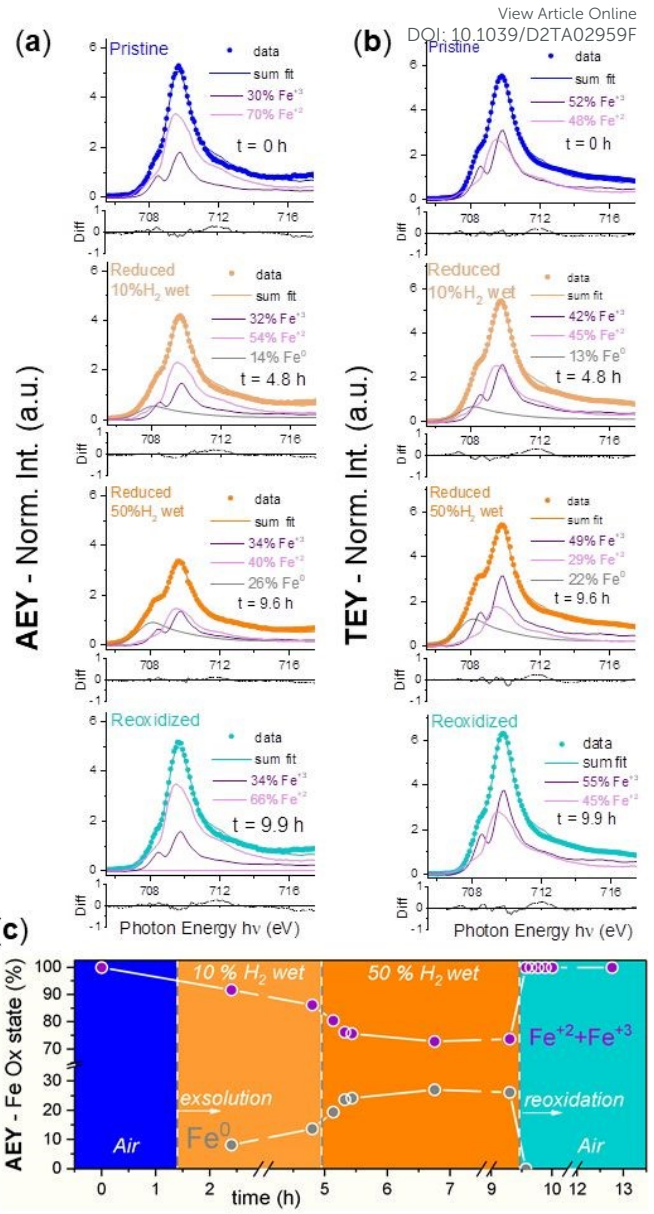

Figure 7 Examples of (a) AEY and (b) TEY normalized NAP-XAS spectra the Fe L_3-edge measured on pristine, reduced (10% and 50% H_2 wet) and reoxidized STFN at the indicated times, together with a linear combination analysis based on spectra of reference (Fe foil, FeO, Fe_2O_3, see Figure S11) compounds, estimating the Fe^{3+}, Fe^{+2} and Fe^0 composition. (c) Time dependent Fe^0 and (Fe^{+2} + Fe^{+3}) compositions obtained from the LCA of all AEY Fe L_3 spectra in each of the specified atmospheres.

3. Discussion

3.1 Surface microstructural modifications induced by exsolution

From the SEM and TEM images and EDS analysis shown in Figure 1.c and the in-situ NAP-XPS spectra given in Figure 4.a, 4.b and 4.f, it is clear that metallic Ni-Fe nanoparticles form under reducing conditions of STFN at 700 ºC. The NAP-XAS analysis in 2.3.3 shows that the complete reduction of Ni^{+2} to Ni^0 occurs immediately after switching to reducing atmospheres, but Fe is reduced only progressively as a function of the pH_2 and of the reduction time (see Figure 7.c tracking the evolution of surface Fe^0 relative to Fe^{+2}/Fe^{+3}). This indicates that Ni reduces easily, dragging out the more stable Fe (The Ellingham diagram shows that Ni reduces more easily than Fe [62]) to form the alloyed Ni-Fe NPs during the exsolution. In this sense, we could say that Ni forms the nucleation sites on which the Fe adds to form the Ni-Fe nanoalloys. On Ni-free STF, Fe is also reduced but this Fe^0 segregation occurs mainly

View Article Online DOI: 10.1039/D2TA02505F

on grain boundaries, forming bigger particles and presenting lower NP area density [23]. Moreover, according to the Fe-Ni phase diagram, at 700 °C, Fe and Ni form a γ face-centered cubic structure solid solution in a wide compositional range,[63] as is also the case for the composition $Ni_{0.7}Fe_{0.3}$ in our nanoparticles, as was determined from the EDS-TEM analysis shown in (Figure 1.c). We also observe that the Fe^0 surface content grows from 14% during reduction in a 10% H_2 atmosphere to a plateau value of ~ 25% that is reached within ~1 h of reduction time in 50% H_2 atmosphere (Figure 7.c). But Fe is never fully reduced, meaning that the perovskite is stable in the applied reducing conditions.

It is also important to consider how exsolution affects the surface segregation of Sr from STFN. Segregation of A-site cations in this type of ABO_3 perovskites is a known phenomenon.[64] In the case of STF, it has been reported that Sr segregation is more prominent with increasing Fe content.[65] However, replacing Fe with more stable transition metals such as Ti also worsens the electrochemical properties, making it less suitable as SOFC electrode.[29] So, in order to mitigate the Sr-segregation during exsolution, an initial Sr-deficiency ($Sr_{0.93}Ti_{0.3}Fe_{0.63}Ni_{0.07}O_{3-\delta}$) was introduced as suggested in ref. [66] for STF. This will also limit the charge unbalance produced by NPs exsolution in Ni-doped STF.[14,21] In spite of this, the chemical structure profile analysis of Sr and O summarized in Figure 5 reveals a slight Sr-surface enrichment during NP exsolution that reverses after reoxidation in the near-surface region but is irreversible in the *termination layer*.

3.2. About the possibility of self-regeneration of electrodes for S-IT-SOFC (symmetric intermediate temperature SOFC)

The possibility of functionalizing perovskites as electrode materials that exsolve NPs for efficient symmetric SOFCs raises the question on whether the material is fully regenerated to its original condition during reoxidation or not. Full reincorporation of the exsolved NPs into the perovskites has been observed for Fe-Co exsolution from $La_{0.8}Sr_{1.2}Fe_{0.9}Co_{0.1}O_{4-\delta}$ (LSFC) after reoxidizing in air at 850 °C for 20 h (the sample was first exsolved at 850 °C in a 5%H_2/N_2 atmosphere), but also nanoparticles that remain in the surface after oxidation were found for Ni-Fe exsolution in $Sr_2Fe_{1.4}Ni_{0.1}Mo_{0.5}O_{6-\delta}$ after reoxidizing in air at 800 °C for 10 h (the sample was exsolved at 800 °C in a 97%H_2/3%H_2O atmosphere)[68]. The first case, in which the original material is recovered, is a very interesting result in order to achieve longer SOFC life-times. However, the second case brings the possibility of also improving the cathode performance when reoxidizing, since the NPs that remain on the surface may become active sites for the ORR. In fact, in references [24,30] Ni exsolution in $Sr_X(Ti,Fe,Ni)O_{3-\delta}$ is aimed at directly as a strategy to improve the cathode performance, taking advantage of this non-reversibility. However, from these previous works it is not clear whether Ni-Fe nanoparticles get oxidized to form a $(Ni,Fe)O_x$ phase, or if Fe is reincorporated into the lattice leaving only NiO particles, or whether a combined scenario (as depicted in **Figure 8**) is most probable.

The results presented in this work, namely (i) the immediate recovery of the Fe L_3-edge XAS spectra when starting reoxidation (compared to pristine, see Figure 7), and (ii) the reoxidized sample having a significantly lower Fe content (TEM-EDS-derived composition, Figure 1) suggest that the Fe from the nanoparticles is indeed reincorporated into the perovskite when reoxidizing, at least to a large extent. As a consequence, the reoxidized nanoparticles are closer in composition to NiO with some substitution of Ni by Fe. This strongly suggests that Fe reincorporation is key for the partial recovery of the material, probably with the formation of a perovskite phase saturated in Sr in the reoxidized near surface layer as depicted in Figure 8. However, the Sr- and O-enrichment in the termination layer after reoxidation and the change in the nature and concentration of the O 1s peak labelled O_{ads} in Figure 5, indicate a certain degree of irreversible surface reorganization. Also, an increased surface roughness is observed for the reoxidized sample in comparison to the STFN pristine (SEM images, Figure 1). The reoxidation

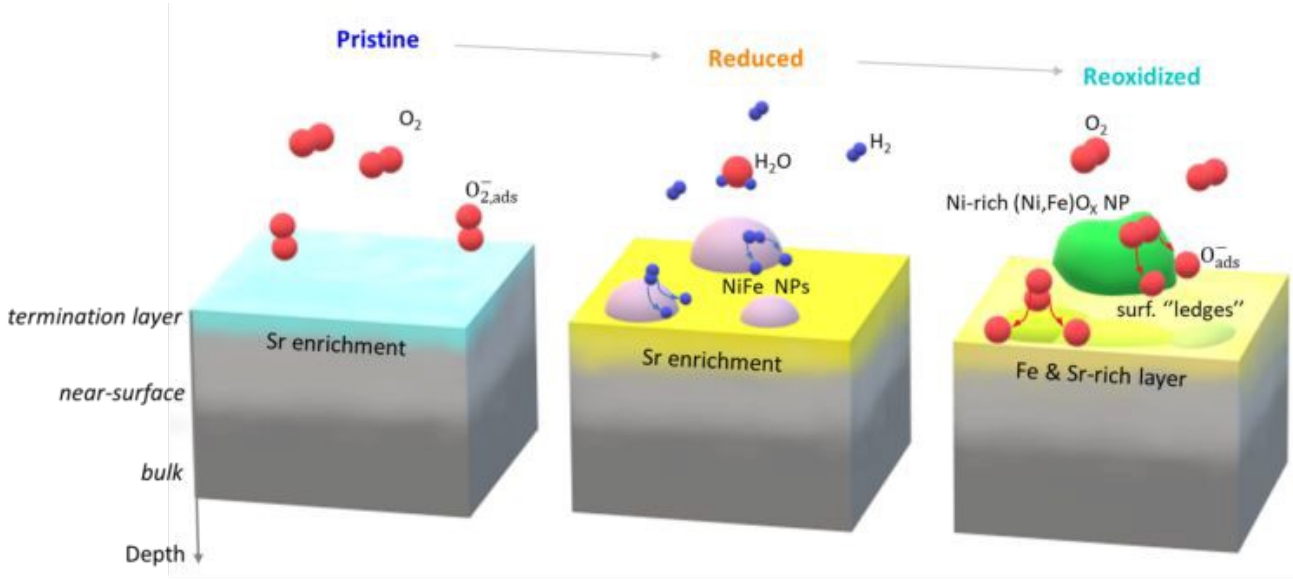

Figure 8 Schematic depiction of the suggested STFN surface reorganization during the atmospheric redox cycle at the solid-gas interface and in depth.

View Article Online DOI: 10.1039/D2TA02505F

process leaves traces in the surface microstructure of the sample, denoted in Figure 8 as "surface ledges". Considering the Sr surface enrichment and Fe partial reincorporation during reoxidation, we propose a reoxidation-induced reconstruction which forms a Fe- and Sr-rich oxide layer in the surface region, leaving the Ni largely segregated from the perovskite. The effect of exsolution-reoxidation on the cathode response is very favorable (Figure 2), showing lower resistance values and a higher frequency in the rate-limiting processes. It can also be seen in Figure 2 that the resistance values grow with reoxidation time at 700 ºC in air. This, along with the slight intensity decrease of the AEY Ni L-edge NAP-XAS spectrum after 3 h reoxidation (Figure 6) and the NP-free surface after 24 h of reoxidation (Figure 1.d), indicates that Ni may also be gradually reincorporated after longer reoxidation times. Thus, lowering the operation temperatures could help to retain the NiO NPs, if desired, for as long as possible on the cathode side.

3.3. Insights on the ORR and HOR mechanisms

In this section, we propose to combine the EIS data and the surface characterization to address questions on the mechanisms for oxygen reduction and hydrogen oxidation reactions (ORR and HOR) on the cathode and anode, respectively.

3.3.1 Oxygen Reduction Reaction. Recently, Mrozinski et al. [69], analyzed the oxygen reduction reactions on undoped $SrTi_{0.3}Fe_{0.7}O_3$ perovskite. The authors proposed an EEC comprised of two RCP subcircuits connected in series. Similar to our results, the low frequency contribution (<10 Hz) was attributed to the O_2 diffusion in the gas phase. As for the higher frequency arc (200-300 Hz at 700 °C in air, E_a ~1.16 eV), the authors suggested a possible surface diffusion followed by a charge transfer reaction limiting step, in accordance with results found for Co-substituted $SrTi_{0.3}Fe_{0.7}O_3$ perovskites reported by Zhang et al.[70] These authors used a Gerischer element to model the high frequency response and found typical activation energies of E_a =1.15-1.3 eV ascribed to a (i) *diffusion process* with low activation energy E_a = 0.68 – 0.8 eV followed by a highly activated (ii) *surface exchange process*, with a surface exchange coefficient E_a =1.98-2.06 eV. In the case of our pristine-STFN we can assume a similar mechanism by considering the similar frequencies and activation energies found for this contribution. However, the surface reorganization induced by the redox cycle produces relevant changes in the EIS spectra, as can be observed from Figure 2: the reoxidized spectra present a significant increase of the characteristic frequency, a ~50% decrease in resistance (at 700°C), and a decrease in activation energy (from 1.36 to 1.05 eV). Ni et al. also found a significant reduction of the polarization resistance (from 0.19 to 0.084 Ω cm^2 at 700 °C) and in its overall activation energy (from 1.256 to 1.146 eV) by in-situ re-oxidation and precipitation of (Ni,Fe)O nanoparticles in the $Sr_{0.95}Ti_{0.3}Fe_{0.6}Ni_{0.1}O_3$ cathode.[30]

We believe that the reduction in activation energy for the Gerischer contribution after surface modification can be explained by an improvement in the surface exchange process, which is consistent with the lower polarization resistance (R_P) values and the shift to higher frequencies after reoxidation (Bode plot in Figure 2). The O_{ads} accumulation observed in the termination layer (Figure 5.b) suggests that the rate-limiting step of the pristine STFN is related to the O_2 adsorption-dissociation. This is in agreement with the high activation energy needed for breaking the O-O bond plus the charge transfer process, and the observed accumulation of $O^-_{2,ads}$ species. Thus, the surface reorganization after the redox cycle seems to facilitate the O_2 adsorption-dissociation; at this stage, the new surface limiting process may be the O-incorporation, limited by the availability of oxygen vacancies in the perovskite lattice and evidenced by the presence of a O^-_{ads} species in the termination layer. Summarizing, the ORR is described in Eq. 1.

$$O_2^{gas} \xrightarrow[RCP]{gas\ dif.} O_{2\ \ close\ to\ surface} \xrightarrow[fast]{adsorption} O_{2\ Ads}^{-,TL} \xrightarrow[G-Pristine]{dissociation} O_{Ads}^{-,TL} \xrightarrow[G-Reoxidized]{incorporation} O^{NS} \xrightarrow[G]{O\ diffusion} O^{bulk} \quad (1)$$

3.3.2 Hydrogen Oxidation Reaction. In perovskite-oxide surfaces, hydrogen adsorbs via an oxidative dissociation with a charge transfer process forming hydroxyl groups ($\mathbf{OH_O}$)[44,45]:

$$\boldsymbol{H_2 + O_O^x \rightleftharpoons OH_O + H_{ad,\,ox} + e'} \quad (2)$$

In this type of MIECs, the process is usually limited by the low amount of oxygen sites for H_2 adsorption to form $\mathbf{H_{ad,\,ox}}$ species. The limitation is due to the high O-vacancy concentration in reducing conditions as it was indicated by NAP-XPS data in Figure 5. For NP-surface functionalized MIEC systems, H_2-dissociative adsorption has been reported to occur more frequently in the NPs giving place to $\mathbf{H_{ad,NP}}$ species, and then diffuse through the NP surface towards the MIEC,[71] where these are adsorbed as $\mathbf{H_{ad,\,ox}}$ species. This process is commonly referred to as hydrogen spillover, and is typical in Ni/YSZ or Ni/GDC composite anodes.[72,73] The adsorption-dissociation process can then be written as:

$$\boldsymbol{H_2 \rightleftharpoons 2H_{ad,NP}} \quad (2'a)$$

And it is followed by an H-atomic diffusion and exchange between NP and the oxide surface:

$$\boldsymbol{H_{ad,NP} \rightleftharpoons H_{ad,\,ox}} \quad (2'b).$$

In relation to this, previous works have compared bare STF with Fe-exsolved-STF [23] and with Ni-Fe exsolved-STFN [14] and observed that bare STF electrodes present a unique LF arc that dominates the anodic response, whereas in NP doped STF/STFN the LF region splits in two arcs (MF & LF as in Figure 3). We believe that this splitting may be a consequence of

View Article Online DOI: 10.1039/D2TA02959F

replacing the H_2 adsorption-dissociation process of Equation (2) with (2'). However, note that the (2') process in STF based electrodes is not comparable to that of Ni/YSZ cermet anodes wherethe O-sites necessary for the (2'b) process are widely available. Note also that the NAP-XPS signal of the O 1s in reducing atmospheres showed no accumulation of $\mathbf{H_2O_{\ddot{O}}}$ or $\mathbf{OH_O}$ on the surface,[74] indicating that processes such as $\mathbf{OH_O}$ recombination or water desorption may be fast enough not to significantly limit the anodic reaction. This is in agreement with previous reports showing that water desorption on perovskite oxides is a very fast process [75]. In conclusion, the previously mentioned H_2 adsorption/dissociation processes (MF+LF region) are the main limiting step in our STFN anode.

4. Conclusions

The STFN electrode was studied as a candidate for symmetric IT-SOFC in a complete redox cycle. The assessment of STFN's potential yielded a good anode performance with Rp of 0.88 Ω.cm^2 at 700 ºC under 10% wet H_2 atmosphere, and a remarkable cathode performance with a Rp of 0.06 Ω.cm^2 at 700 ºC in air (lowered to 0.04 Ω.cm^2 after exsolution/reoxidation). It was revealed that in reducing atmosphere Ni exsolves quickly, reducing fully from Ni^{+2} to the metallic state Ni^0, whereas Fe remains as a combination of oxidation states, with Fe^{+2}/Fe^{+3} in the perovskite and Fe^0 in the NPs. The amount of Fe^0 on the surface increases with increasing H_2 content in the reducing atmosphere and reduction time until a plateau value is reached. So, under the applied reducing conditions Ni reduces totally, dragging out the more stable Fe to alloy in the metallic nanoparticles of approximate composition ~$Ni_{0.7}Fe_{0.3}$. Exsolution results in a detectable Sr-enrichment towards the solid-gas interface in the STFN termination layer to compensate for the necessary B-site cation loss from the perovskite. The negative effect that one could expect from the surface Sr-segregation is reduced by the Sr deficiency of the pristine perovskite, and then after exsolution overruled by the great catalytic activity of the Fe-Ni nanoparticles. Overall, after the redox cycle, the surface Sr-enrichment is irreversible in the "termination layer" but seemingly reversible in the near surface region underneath. There is also a clear reversibility in the Fe oxidation state during reoxidation, and the NP composition ($Ni_{0.9}Fe_{0.1}$)O has a richer Ni:Fe ratio after reoxidation. The microstructure of reoxidized STFN is different from that of the pristine sample. Reoxidized STFN has coarser grains, surface "ledges" and some remaining oxidized nanoparticles. Thus, we propose a surface reconstruction of the electrode induced by reoxidation, forming a Fe- and Sr-rich layer near the surface, while leaving the Ni segregated from the perovskite forming Ni-rich (Ni, Fe)O nanoparticles of NiO structure. We observed that the reoxidized sample shows a quite different EIS cathode response compared to the pristine sample, with a different mechanism for the ORR in the reoxidized electrode, with O-diffusion/$O_{2,ads}$ dissociation being the main limiting step in the pristine sample, and O-diffusion/O_{Ads}-incorporation in the reoxidized case. This is corroborated by the observed changes in the O 1s NAP-XPS spectra of pristine and reoxidized STFN, in which different O_{Ads} surface species were revealed.

5. Experimental

5.1 Sample preparation and structural characterization

STFN was prepared by a previously described[23] glycine combustion sol-gel method . Titanium butoxide ($C_{16}H_{36}O_4Ti$), $SrCO_3$, $Fe(NO_3)_3.9H_2O$ and $Ni(NO_3)_2.6H_2O$ were used as starting materials to obtain $Sr_{0.93}Ti_{0.3}Fe_{0.63}Ni_{0.07}O_{3-d}$. Once the gel was ignited, the resulting powder was treated at 850 °C for 6 h in air. STFN pellets of 6 mm diameter were cold-pressed and then sintered at 1000°C for 4 h in air. The desired phases, as well as phase stability after 4 h reduction at 700 °C in a humidified atmosphere containing 50 %H_2, were confirmed by conducting powder X-ray diffraction (XRD) on a Panalytical Empyrean using Cu K_α radiation, a graphite monochromator, and a PIXcel detector (see diffractograms in Figure S2, Supplementary Information). The evolution of the electrode microstructure and local composition after different treatments were analyzed by scanning and transmission electron microscopies and energy dispersive X-ray spectroscopy (SEM and TEM+EDS), using a Zeiss Crossbeam 340 and a FEI TECNAI F20 microscopes, respectively.

Symmetrical cells of 1 cm diameter were fabricated with 30 µm thick porous STFN electrodes, 0.8 mm thick dense LSGM ($La_{0.8}Sr_{0.2}Ga_{0.8}Mg_{0.2}O_3$, supplied by 'Fuel Cell Materials', France) electrolyte and a ~4 µm thick LDC (La-doped ceria, $La_{0.6}Ce_{0.4}O_{2-\delta}$) buffer layer. The resulting configuration was STFN/LDC/LSGM/LDC/STFN. The LDC powder was obtained by solid-state reaction mixing stoichiometric amounts of La_2O_3 and CeO_2, whereas the LSGM powder was uniaxially pressed into pellets, and then both were heat treated at 1450°C for 6 h in air. Afterwards, a LDC ink was prepared by admixing 5% PVB and 2.5% PVP as binders, and a solution of 70% α-Terpineol – 110% isopropyl alcohol as dispersing agents. The LDC ink was spin coated over the LSGM electrolyte surface and then fired at 1450 °C for 6 h in air. A STFN ink was prepared with the same procedure and was spin coated onto the LDC buffer layer to complete the cells that were finally treated at 1000 °C for 1.5 h in air. A silver paste grid was painted on top of the electrodes, and gold grids were used on top as current collectors.

5.2 Thermochemical analysis

A thermogravimetric (TG) analysis was performed on a symmetrical thermobalance consisting of a Cahn 1000 electrobalance able to detect mass changes with a precision of up to 10 µg as a function of time.[76] Pristine STFN powder was heated at 5 ºC min^{-1} in air up to 700 °C for an isothermal redox cycle. After purging with inert Ar for > 3 h, the sample was reduced in a humidified atmosphere containing 10% H_2 balanced by Ar for 4 h followed by a second Ar purge. Finally, the sample was reoxidized in synthetic air for 18 h. In all cases, the gas flow rate was 100 ml min^{-1}.

Temperature programmed reductions (TPR) were performed in a Micromeritics Chemisorb 2750 equipment that determines

View Article Online
DOI: 10.1039/D2TA02959F

the H_2 uptake from the sample with a thermal conductivity detector. Powder samples were pre-treated in pure He flow at 300 °C for 1 h to remove adsorbed species. Reductions were carried out from room temperature up to 900 °C by heating at 10 °C min^{-1} under a 50 ml min^{-1} flow of 5% H_2 balanced by Ar on both, STFN and STF samples for comparison.

5.3 Electrochemical characterization

Electrochemical impedance spectroscopy (EIS) measurements were performed on the symmetrical cells using an Autolab PGSTAT32 with a frequency analyzer (FRA2) module in the frequency range from 1 MHz to 10 mHz applying an AC perturbation of 10 mV amplitude and zero DC bias.

EIS spectra were acquired while following a redox cycle, first at ambient pressure in synthetic air, i.e. as cathode, as a function of temperature up to 700 °C, condition referred to as pristine as for TG. Afterwards, the atmosphere was purged with inert Ar gas and then switched to 10%H_2:3%H_2O:87%Ar to reduce the electrode at 700 °C for 45 min, thus producing the exsolution. EIS spectra of the reduced electrode were collected within 700 – 550 °C to characterize the temperature dependent response of the STFN electrode as anode. To complete the redox cycle, the atmosphere was purged with Ar at 400 °C and finally, the atmosphere was switched back to air for EIS spectra to be collected in the reoxidized condition up to 700 °C and there, after 1 h, 6 h and 24 h of reoxidation. All EIS spectra were normalized by the cell geometric area and divided by two in order to account for the symmetrical configuration. EIS data was fitted with electrical equivalent circuits (EEC) using an open source Matlab code.[77] Distribution relaxation time (DRT) calculations were performed with the open source DRTtools software, developed by the Ciucci group,[78] using Gaussians for the radial basis functions (RBF). The adopted FWHM was 0.4, considering that the EIS experiments were measured with 5 frequencies per decade. The selected value for the regularization parameter was 10^{-3}.

5.3 Synchrotron-based X-ray spectroscopy studies

In-situ NAP-XPS and NAP-XAS measurements were conducted on STFN pellets in pristine, reduced and reoxidized conditions at the MPG BElChem UE56/2-PGM1 beamline of HZB's BESSY II synchrotron facility. In BElChem, the soft X-ray beam is refocused after the exit slit (180 μm) to ensure a highly brilliant spot at the sample position. A thin SiN_x membrane separates the beamline from the reaction chamber. A differentially pumped hemispherical SPECS Phoibos 150 NAP electron analyzer was used. A positive potential was applied to the analyzer to suppress gas related peaks detection.[79] Further details of the setup can be found in references.[80,81] Stainless steel plates clamp the pellets onto a sapphire holder. A thin thermocouple measured the temperature on the analyzed side of the pellets that were laser-heated from the backside at 10 °C min^{-1} up to 700 °C. All experiments were performed at a pressure of 0.5 mbar, initially in an oxidizing (20%O_2:80%N_2) environment, then in mild (10%H_2:87%N_2:3%H_2O) followed by stronger (50%H_2:47%N_2:3%H_2O) reducing conditions, and completing the redox cycle in a reoxidizing (20%O_2:80%N_2) atmosphere. The chamber was evacuated down to 10^{-5} mbar within a few seconds between atmospheric changes.

Detail spectra of Sr 3d, C 1s/Sr 3p, Ti 2p, O 1s, Fe 2p and Fe 2s/Ni 2p core levels were acquired with 260, 420, 610, 700, 860 and 1010 eV photon energies, respectively, to produce photoelectrons of about 150 eV kinetic energy, ensuring surface sensitivity and same probing depth for all elements. Additional photon energies (510 and 810 eV) for Sr 3d and (950 and 1250 eV for) O 1s corresponding to photoelectrons having 400 and 700 eV kinetic energies, respectively, were applied for depth-dependent information. Inelastic Mean Free Paths (IMFP) were calculated using the NIST Database[82] according to Tanuma, Power and Penn.[49] Valence band spectra and shallow core levels were acquired with 200 eV photon energy. The binding energy was calibrated by referencing the Fermi edge of a clean Ir foil to 0.0 eV for all photon energies. 20 eV pass energy and 0.1 eV step size were used to collect the spectra. Detailed information on the fit analysis of the Sr 3d and O 1s spectra is given in section S4.2 of SI.

NAP-XAS spectra were collected both in Auger electron yield (AEY) and total electron yield (TEY) modes. Photon energies were calibrated by the Fermi edge of Ir for the used pass energy of 50 eV. Spectra were then normalized by a step-like background, using the software Athena,[55] that also allowed for a Linear Combination Analysis (LCA) of the Fe L_3-edge using Fe^0, Fe^{+2} and Fe^{+3} references. For further information on the LCA see section S4.3 of SI.

Author Contributions

LVM, HET and CEJ conceived the project.

LVM, MB, CEJ, AK-G, MDA and HET acquired the financial support and or provided main resources.

MS synthesized the materials and fabricated the cells for EIS, performed EIS experiments and analyzed the EIS data with LVM.

CEJ, MS, EAC and RG-D conducted the in-situ synchrotron NAP-XPS/XAS experiments. RG-D performed the NAP-XPS/XAS data reduction and ex-situ HAXPES measurements with RGW.

CEJ analyzed XPS spectra with advice of RGW and MB. MDA did the complementary NAP-XPS analysis in S4.1.

MS and CEJ analyzed the XAS data.

MS conducted XRD, TEM/EDS/SEM with HET, TG with LVM, and analyzed the data. LMT conducted TPR and analyzed the data with MS.

LVM, CEJ, MS, HET, MDA and LMT discussed and rationalized the data.

MS and CEJ wrote the main manuscript and prepared the figures. All authors revised and corrected the manuscript.

Conflicts of interest

There are no conflicts to declare.

Acknowledgements

View Article Online
DOI: 10.1039/D2TA03059F

Authors MS, HET, MDA, LMT and LVM acknowledge funding from Consejo Nacional de Investigaciones Científicas y Técnicas (CONICET) Grant PIP-67595, the Agencia Nacional de Promoción de Ciencia y Tecnología (ANPCyT) Grant PICT 2019-03721 and the Comisión Nacional de Energía Atómica (CNEA) Grant PAC 2019-2020. Author MS acknowledges CONICET for a PhD grant and the HZB Photon School for a travel grant. We also thank the FHI for beamtime allocation at the UE56/2-PGM1 beamline, BElChem, hosted at BESSY II synchrotron light source. We acknowledge Bernardo Pentke and Alberto Baruj for SEM analysis assistance as well as Kaiqi Nie and Wanli Yang for providing Fe L-edge XAS reference spectra. The collection of the XAS spectra used resources of the Advanced Light Source, which is a DOE Office of Science User Facility under contract no. DE-AC02-05CH11231. We also acknowledge Ueda Shigenori for assistance in the collection of Sr 3d HAXPES spectra at the BL15XU beamline of the SPring-8 synchrotron facility in Japan. The authors declare no competing financial interest.

Notes and references

1 IEA, Futur. Hydrog., https://www.iea.org/reports/the-future-of-hydrogen.

2 IEA, Technology Roadmap - Hydrogen and Fuel Cells, https://www.iea.org/reports/technology-roadmap-hydrogen-and-fuel-cells.

3 C. Zhao, Y. Li, W. Zhang, Y. Zheng, X. Lou, B. Yu, J. Chen, Y. Chen, M. Liu and J. Wang, *Energy Environ. Sci.*, 2020, **13**, 53–85.

4 H. Su and Y. H. Hu, *Chem. Eng. J.*, 2020, **402**, 126235.

5 L. Zhang, Y. Xing, H. Xu, H. Wang, J. Zhong and J. Xuan, *Energy Convers. Manag.*, 2017, **139**, 79–88.

6 B. Yildiz, in *Functional Materials for Sustainable Energy Applications*, Elsevier, 2012, pp. 149-179e.

7 Z. Gao, L. V. Mogni, E. C. Miller, J. G. Railsback and S. A. Barnett, *Energy Environ. Sci.*, 2016, **9**, 1602–1644.

8 D. Burnat, R. Kontic, L. Holzer, P. Steiger, D. Ferri and A. Heel, *J. Mater. Chem. A*, 2016, **4**, 11939–11948.

9 J. Hwang, R. R. Rao, L. Giordano, Y. Katayama, Y. Yu and Y. Shao-Horn, *Science (80-.).*, 2017, **358**, 751–756.

10 W. T. Hong, M. Risch, K. A. Stoerzinger, A. Grimaud, J. Suntivich and Y. Shao-Horn, *Energy Environ. Sci.*, 2015, **8**, 1404–1427.

11 P. Kaur and K. Singh, *Ceram. Int.*, 2020, **46**, 5521–5535.

12 L. Shu, J. Sunarso, S. S. Hashim, J. Mao, W. Zhou and F. Liang, *Int. J. Hydrogen Energy*, 2019, **44**, 31275–31304.

13 Y. Li, K. Xie, S. Chen, H. Li, Y. Zhang and Y. Wu, *Electrochim. Acta*, 2015, **153**, 325–333.

14 T. Zhu, H. E. Troiani, L. V. Mogni, M. Han and S. A. Barnett, *Joule*, 2018, **2**, 478–496.

15 J. Li, Y. Yu, Y.-M. Yin, N. Zhou and Z.-F. Ma, *Electrochim. Acta*, 2017, **235**, 317–322.

16 D. Neagu, T.-S. Oh, D. N. Miller, H. Ménard, S. M. Bukhari, S. R. Gamble, R. J. Gorte, J. M. Vohs and J. T. S. Irvine, *Nat. Commun.*, 2015, **6**, 8120.

17 J. Myung, D. Neagu, D. N. Miller and J. T. S. Irvine, *Nature*, 2016, **537**, 528–531.

18 O. Kwon, S. Sengodan, K. Kim, G. Kim, H. Y. Jeong, J. Shin, Y.-W. Ju, J. W. Han and G. Kim, *Nat. Commun.*, 2017, **8**, 15967.

19 Y.-F. Sun, J.-H. Li, L. Cui, B. Hua, S.-H. Cui, J. Li and J.-L. Luo, *Nanoscale*, 2015, **7**, 11173–11181.

20 D. Neagu, G. Tsekouras, D. N. Miller, H. Ménard and J. T. S. Irvine, *Nat. Chem.*, 2013, **5**, 916–923.

21 T. Zhu, H. Troiani, L. V. Mogni, M. Santaya, M. Han and S. A. Barnett, *J. Power Sources*, 2019, **439**, 227077.

22 J. Song, T. Zhu, X. Chen, W. Ni and Q. Zhong, *J. Mater.*, 2020, **6**, 377–384.

23 M. Santaya, L. Toscani, L. Baqué, H. E. Troiani and L. Mogni, *Solid State Ionics*, 2019, **342**, 115064.

24 G. Yang, W. Zhou, M. Liu and Z. Shao, *ACS Appl. Mater. Interfaces*, 2016, **8**, 35308–35314.

25 T. Götsch, N. Köpfle, M. Grünbacher, J. Bernardi, E. A. Carbonio, M. Hävecker, A. Knop-Gericke, M. F. Bekheet, L. Schlicker, A. Doran, A. Gurlo, A. Franz, B. Klötzer and S. Penner, *Phys. Chem. Chem. Phys.*, 2019, **21**, 3781–3794.

26 Y. Gao, D. Chen, M. Saccoccio, Z. Lu and F. Ciucci, *Nano Energy*, 2016, **27**, 499–508.

27 A. Nenning, A. K. Opitz, C. Rameshan, R. Rameshan, R. Blume, M. Hävecker, A. Knop-Gericke, G. Rupprechter, B. Klötzer and J. Fleig, *J. Phys. Chem. C*, 2016, **120**, 1461–1471.

28 J. C. Ruiz-Morales, D. Marrero-López, J. Canales-Vázquez and J. T. S. Irvine, *RSC Adv.*, 2011, **1**, 1403.

29 S.-L. Zhang, D. Cox, H. Yang, B.-K. Park, C.-X. Li, C.-J. Li and S. A. Barnett, *J. Mater. Chem. A*, 2019, **7**, 21447–21458.

30 W. Ni, T. Zhu, X. Chen, C. Jin, Y. Bu, Q. Zhong and M. Han, *J. Power Sources*, 2021, **489**, 229490.

31 M. Santaya, H. E. Troiani, A. Caneiro and L. V Mogni, *ACS Appl. Energy Mater.*, 2020, **3**, 9528–9533.

32 E. J. Crumlin, E. Mutoro, Z. Liu, M. E. Grass, M. D. Biegalski, Y.-L. Lee, D. Morgan, H. M. Christen, H. Bluhm and Y. Shao-Horn, *Energy Environ. Sci.*, 2012, **5**, 6081.

33 Y. Wen, T. Yang, D. Lee, H. N. Lee, E. J. Crumlin and K. Huang, *J. Mater. Chem. A*, 2018, **6**, 24378–24388.

34 D. Neagu, E. I. Papaioannou, W. K. W. Ramli, D. N. Miller, B. J. Murdoch, H. Ménard, A. Umar, A. J. Barlow, P. J. Cumpson, J. T. S. Irvine and I. S. Metcalfe, *Nat. Commun.*, 2017, **8**, 1855.

35 E. Barsoukov and J. R. Macdonald, Eds., *Impedance Spectroscopy*, Wiley, 2005.

36 S. B. Adler, J. A. Lane and B. C. H. Steele, *J. Electrochem. Soc.*, 1996, **143**, 3554–3564.

37 F. Liu, L. Zhang, G. Huang, B. Niu, X. Li, L. Wang, J. Zhao and Y. Jin, *Electrochim. Acta*, 2017, **255**, 118–126.

38 X. Meng, Y. Wang, Y. Zhao, T. Zhang, N. Yu, X. Chen, M. Miao and T. Liu, *Electrochim. Acta*, 2020, **348**, 136351.

39 Y. Cao, Z. Zhu, Y. Zhao, W. Zhao, Z. Wei and T. Liu, *J. Power Sources*, 2020, **455**, 227951.

40 P. I. Cowin, R. Lan, C. T. G. Petit and S. Tao, *Solid State Sci.*, 2015, **46**, 62–70.

41 A. Rothschild, W. Menesklou, H. L. Tuller and E. Ivers-Tiffée, *Chem. Mater.*, 2006, **18**, 3651–3659.

42 A. Nenning, L. Volgger, E. Miller, L. V. Mogni, S. Barnett and J. Fleig, *J. Electrochem. Soc.*, 2017, **164**, F364–F371.

43 L. dos Santos-Gómez, J. M. Compana, S. Bruque, E. R. Losilla and D. Marrero-López, *J. Power Sources*, 2015, **279**, 419–427.

44 T. Zhu, D. E. Fowler, K. R. Poeppelmeier, M. Han and S. A. Barnett, *J. Electrochem. Soc.*, 2016, **163**, F952–F961.

45 M. Chen, D. Chen, M. Chang, H. Hu and Q. Xu, *J. Electrochem. Soc.*, 2017, **164**, F405–F411.

46 D. E. Fowler, J. M. Haag, C. Boland, D. M. Bierschenk, S. A. Barnett and K. R. Poeppelmeier, *Chem. Mater.*, 2014, **26**, 3113–3120.

47 L. Bian, C. Duan, L. Wang, L. Zhu, R. O'Hayre and K.-C. Chou, *J. Power Sources*, 2018, **399**, 398–405.

48 Z. Du, H. Zhao, S. Yi, Q. Xia, Y. Gong, Y. Zhang, X. Cheng, Y. Li, L. Gu and K. Świerczek, *ACS Nano*, 2016, **10**, 8660–8669.

49 S. Tanuma, C. J. Powell and D. R. Penn, *J. Electron Spectros. Relat. Phenomena*, 1990, **52**, 285–291.

50 M. Ghaffari, T. Liu, H. Huang, O. K. Tan and M. Shannon, *Mater. Chem. Phys.*, 2012, **136**, 347–357.

51 A. K. Opitz, C. Rameshan, M. Kubicek, G. M. Rupp, A. Nenning, T. Götsch, R. Blume, M. Hävecker, A. Knop-Gericke, G. Rupprechter, B. Klötzer and J. Fleig, *Top. Catal.*, 2018, **61**, 2129–2141.

52 P. A. W. van der Heide, *Surf. Interface Anal.*, 2002, **33**, 414–425.

53 J.-C. Dupin, D. Gonbeau, P. Vinatier and A. Levasseur, *Phys. Chem. Chem. Phys.*, 2000, **2**, 1319–1324.

54 L. L. Ding, L. Q. Wu, X. S. Ge, Y. N. Du, J. J. Qian, G. D. Tang and W. Zhong, *Results Phys.*, 2018, **9**, 866–870.

55 B. Ravel and M. Newville, *J. Synchrotron Radiat.*, 2005, **12**, 537–541.

56 M. L. Medarde, *J. Phys. Condens. Matter*, 1997, **9**, 1679–1707.

57 D. J. Watson, S. Acharya, R. E. J. Nicklin and G. Held, *Surf. Sci.*, 2014, **629**, 108–113.

58 T. Jo and A. Tanaka, *J. Electron Spectros. Relat. Phenomena*, 2001, **117–118**, 397–411.

59 J. Stöhr, *NEXAFS Spectroscopy*, Springer Berlin Heidelberg, Berlin, Heidelberg, 1992, vol. 25.

60 P. S. Miedema and F. M. F. de Groot, *J. Electron Spectros. Relat. Phenomena*, 2013, **187**, 32–48.

61 E. O. Filatova, Y. V. Egorova, K. A. Galdina, T. Scherb, G. Schumacher, H. J. M. Bouwmeester and S. Baumann, *Solid State Ionics*, 2017, **308**, 27–33.

62 H. J. T. Ellingham, *Vacuum*, 1959, **7–8**, 216.

63 The Materials Information Society, *Bull. Alloy Phase Diagrams*, 1982, **3**, 376–402.

64 B. Koo, K. Kim, J. K. Kim, H. Kwon, J. W. Han and W. Jung, *Joule*, 2018, **2**, 1476–1499.

65 W. Jung and H. L. Tuller, *Energy Environ. Sci.*, 2012, **5**, 5370–5378.

66 D. P. Fagg, V. V. Kharton, A. V. Kovalevsky, A. P. Viskup, E. N. Naumovich and J. R. Frade, *J. Eur. Ceram. Soc.*, 2001, **21**, 1831–1835.

67 J. Zhou, T.-H. Shin, C. Ni, G. Chen, K. Wu, Y. Cheng and J. T. S. Irvine, *Chem. Mater.*, 2016, **28**, 2981–2993.

68 T. Liu, Y. Zhao, X. Zhang, H. Zhang, G. Jiang, W. Zhao, J. Guo, F. Chen, M. Yan, Y. Zhang and Y. Wang, *J. Mater. Chem. A*, 2020, **8**, 582–591.

69 A. Mroziński, S. Molin and P. Jasiński, *Electrochim. Acta*, 2020, **346**, 136285.

70 S.-L. Zhang, H. Wang, M. Y. Lu, A.-P. Zhang, L. V. Mogni, Q. Liu, C.-X. Li, C.-J. Li and S. A. Barnett, *Energy Environ. Sci.*, 2018, **11**, 1870–1879.

71 A. K. Opitz, A. Nenning, V. Vonk, S. Volkov, F. Bertram, H. Summerer, S. Schwarz, A. Steiger-Thirsfeld, J. Bernardi, A. Stierle and J. Fleig, *Nat. Commun.*, 2020, **11**, 4801.

72 M. Vogler, A. Bieberle-Hütter, L. Gauckler, J. Warnatz and W. G. Bessler, *J. Electrochem. Soc.*, 2009, **156**, B663.

73 V. Sharma, P. A. Crozier, R. Sharma and J. B. Adams, *Catal. Today*, 2012, **180**, 2–8.

74 N. A. Merino, B. P. Barbero, P. Eloy and L. E. Cadús, *Appl. Surf. Sci.*, 2006, **253**, 1489–1493.

75 A. Nenning, E. Navickas, H. Hutter and J. Fleig, *J. Phys. Chem. Lett.*, 2016, **7**, 2826–2831.

76 A. Caneiro, P. Bavdaz, J. Fouletier and J. P. Abriata, *Rev. Sci. Instrum.*, 1982, **53**, 1072–1075.

77 Jean-Luc Dellis., Zfit, MATLAB Central File Exchange, https://www.mathworks.com/matlabcentral/fileexchange/19460-zfit.

78 T. H. Wan, M. Saccoccio, C. Chen and F. Ciucci, *Electrochim. Acta*, 2015, **184**, 483–499.

79 B. Junker, M. Favaro, D. E. Starr, M. Hävecker, U. Weimar and N. Barsan, *J. Phys. D. Appl. Phys.*, 2022, **55**, 064002.

80 A. Knop-Gericke and M. Havecker, ISISS, BElChem, and CAT@EMIL facilities, http://www.fhi-berlin.mpg.de/acnew/groups/electronicstructure/pages/beamline.html.

81 H. Bluhm, M. Hävecker, A. Knop-Gericke, M. Kiskinova, R. Schlögl and M. Salmeron, *MRS Bull.*, 2007, **32**, 1022–1030.

82 C. J. Powell and A. Jablonski, NIST Electron Inelastic-Mean-Free-Path Database, http://www.nist.gov/srd/surface.cfm.